Systematic investigation of anomalous Hall effect in Fe-Pt composition-spread epitaxial films for magnetic sensor application

Akhilesh Kumar Patel[1], Ryo Toyama[1], Keisuke Masuda[1], Kodchakorn Simalaotao[1,2], Tomoya Nakatani[1], Yoshio Miura[1,3], and Yuya Sakuraba[1,2]*

[1]Research Center for Magnetic and Spintronic Materials, National Institute for Materials Science (NIMS), 1-2-1 Sengen, Tsukuba, Ibaraki 305-0047, Japan

[2]Graduate School of Pure and Applied Sciences, University of Tsukuba, Tennodai, Tsukuba, Ibaraki 305-8571, Japan

[3]Faculty of Electrical Engineering and Electronics, Kyoto Institute of Technology, Hashikami-cho, Matsugasaki, Sakyo-ku, Kyoto 606-8585, Japan

mailto:

*Corresponding author: SAKURABA.Yuya@nims.go.jp

ABSTRACT

Magnetic field sensors based on the anomalous Hall effect (AHE) requires a magnetic thin film with a high anomalous Hall resistivity (ρ_{yx}^{A}) and moderate perpendicular uniaxial magnetic anisotropy (K_u) to achieve both a large linear sensitivity and a dynamic range (*DR*) adaptable for various applications. In this study, we fabricate $Fe_{1-x}Pt_x$ ($0 \leq x \leq 1$) composition-spread epitaxial thin films and systematically investigate the composition dependence of AHE, aiming to achieve high sensitivity for the magnetic field sensors. We also explore the underlying physical mechanism of AHE in the Fe-Pt binary system. Structural analysis reveals the [001]-oriented epitaxial growth, featuring distinct phases of *A*2-Fe, $L1_2$-Fe_3Pt, $L1_0$-FePt, and $L1_2$-$FePt_3$ as increasing *x* along with their mixed-phases , except for the Pt rich region. Among the entire $Fe_{1-x}Pt_x$, an off-stoichiometric Fe-rich composition $Fe_{0.70}Pt_{0.30}$ exhibits the highest ρ_{yx}^{A} of 4.5 μΩ cm with a linear response to the external magnetic field and a DR of 600 mT, yielding a high sensitivity of 8 μΩ cm/T. The anomalous Hall conductivity (AHC) shows an oscillatory variation with composition x, with the largest AHC of 1261 S/cm observed for $Fe_{0.70}Pt_{0.30}$. The theoretical calculation of the AHC for $A2$-Fe and $L1_2$-Fe_3Pt including the analysis of the density of states for the off-stoichiometric compositions, suggests that the overall variation in AHC with x can be mostly explained by an intrinsic mechanism and the electron doping effect introduced by Pt addition. The theoretical analysis supports that the highest sensitivity obtained in $Fe_{0.70}Pt_{0.30}$ originates from the large intrinsic AHC (1759 S/cm) predicted for the $L1_2$-Fe_3Pt.

I. INTRODUCTION

Research on materials with large anomalous Hall effect (AHE) has attracted significant attention from the viewpoints of fundamental physics and potential applications. Regarding the applications, Magnetic sensors based on the AHE (hereafter referred to as AHE sensors) have been studied extensively.[1–5] The AHE sensors offer several advantages over ordinary Hall effect (OHE)-based sensors, including a wider operational frequency range, lower temperature dependence, and reduced intrinsic noise due to smaller sensor resistance.[6,7] It has also been proposed that the AHE sensors could be used as read head sensors for hard disc drives, offering superior scalability compared to sensors based on the giant magnetoresistance and tunnel magnetoresistance.[8] The AHE sensors operate with the linear change of anomalous Hall voltage with magnetic field, driven by a variation of magnetization direction from in-plane to out-of-plane in the magnetic thin film. Depending on the specific sensor application the sensitivity ($S = \rho_{yx}^{A}/H_s$) and the dynamic range

(DR = $2H_s$) need to be optimized, where ρ_{yx}^{A} is the anomalous hall resistivity (AHR) and H_s is the saturation field. This can be achieved by tuning two dominant magnetic anisotropies in the magnetic thin films: the uniaxial perpendicular magnetic anisotropy energy (K_u) and demagnetization energy ($M_s^2\mu_0/2$), where M_s and μ_0 denote the saturation magnetization and the magnetic permeability, respectively. Figure 1 presents a schematic of AHE curves in the magnetic thin film, illustrating three cases based on the relative magnitudes of K_u and M_s; (Case I) $|K_u|$ is much smaller than $M_s^2\mu_0/2$, yielding the H_s nearly equal to M_s/μ_0, (Case II) K_u is negative with $|K_u|$ much larger than $M_s^2\mu_0/2$ and (Case III) K_u is negative with $|K_u|$ comparable to $M_s^2\mu_0/2$. In Case II, the film normal direction becomes a strong easy-axis magnetization, resulting in a hysteresis loop, which is undesirable for magnetic sensor applications. Consequently, because the *DR* and *S* have a trade-off relationship through H_s, it is important to explore the material with appropriate values of K_u and M_s to achieve optimum *DR* while avoiding the hysteresis loop in Case III. Additionally, to maximize *S* without compromising *DR*, using materials with a higher ρ_{yx}^{A} is crucial.

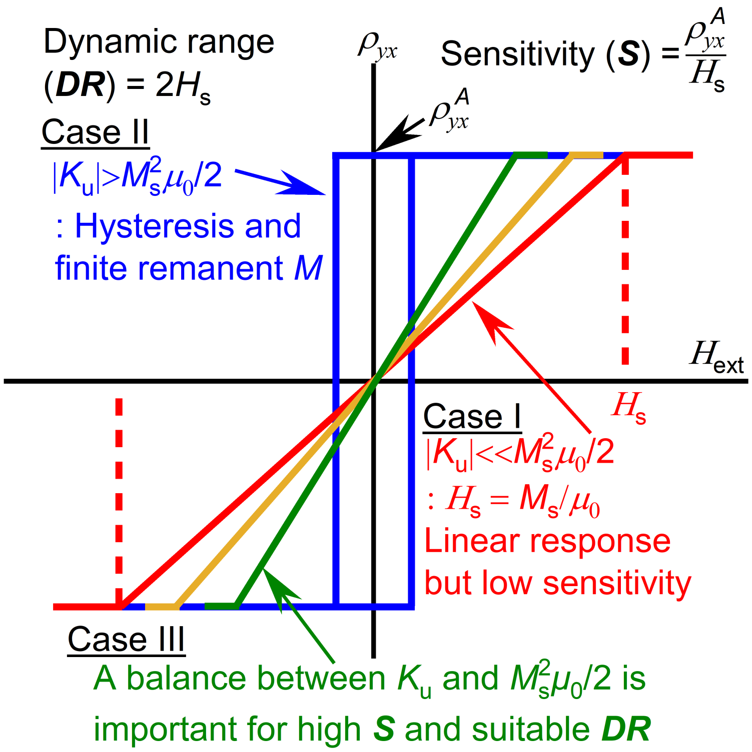

Fig. 1. Schematic diagram for magnetic field (H_{ext}) dependent Hall resistivity (ρ_{yx}), balancing magnetic anisotropy and demagnetization energies to get suitable *S* and *DR*.

For obtaining large ρ_{yx}^A, materials exhibiting giant AHE due to their intrinsic large Berry curvatures, such as Co_2MnGa, Co_2MnAl, Fe_3Sn_2, Mn_3Sn, Fe_3Ga, $Fe_{0.81}Al_{0.19}$ and GdFeCo are promising candidates.[9–16] For example, *S* and *DR* for an epitaxial Co_2MnAl film[10] with ρ_{yx}^A of 18 $\mu\Omega$cm and a saturation field of 1 T are estimated to be 18 $\mu\Omega$cm/T and 2000 mT, respectively. However, although it is a potential way to enhance the *S* further by tuning the *DR* to meet the requirement for specific sensor applications, these soft-magnetic materials lack the tunability of *DR* because of their small K_u. Zhu et al. reported very large *S* around 23760 Ω/T (28500 μΩ cm/T) and a small *DR* of 3 mT in the ultra-thin CoFeB(1.2 nm)/MgO film by using the large $|K_u|$ originating from interfacial magnetic anisotropy and making the balance with $M_s^2\mu_0/2$.[17] However, the high longitudinal resistance of ultrathin films increases noise, which may degrade signal-to-noise ratio of the AHE sensor. In addition, the control of the interfacial magnetic anisotropy of ultrathin films is highly process-sensitive and temperature dependent,[18] presenting significant challenges for reliable sensor use. Therefore, finding materials with a large *S* and an appropriate *DR* at room temperature remains challenging. A material system with not only large ρ_{yx}^{A} but also tunable $|K_\mathrm{u}|$ due to intrinsic crystalline magnetic anisotropy is promising for advancing AHE sensors.

The Fe-Pt binary ordered alloy system is an attractive candidate for achieving both large *S* and tunability in *DR*. $L1_2$-Fe_3Pt, in particular, has been reported to exhibit a large anomalous Hall conductivity (AHC) of 1926 S/cm, more than two times larger than that of $L1_0$-FePt (830 S/cm), while the value of K_u of $L1_2$-Fe_3Pt (4×10^6 erg/cc) is an order of magnitude smaller than that of $L1_0$-FePt (5×10^7 erg/cc).[19,20] In addition, $L1_2$-Fe_3Pt has a similar structure to $L1_0$-FePt (the center site of the Pt layer in $L1_0$-FePt is replaced with Fe atom). Therefore, by tunning the composition ratio of Fe:Pt from $L1_2$-Fe_3Pt to $L1_0$-FePt region, it is expected to achieve large *S* due to large ρ_{yx}^{A} and tunable *DR* across a wide magnetic field range. Most of the prior research on the AHE sensors involving Fe-Pt compositions has focused on Pt-rich compositions[7,21,22], however no study on Fe-rich compositions has been reported to date.

In this study, we systematically investigated the dependence of the crystal structure and transport properties including AHE on Fe-Pt binary alloy system, covering the full range from pure Fe to pure Pt. In order to study the composition dependence of AHE in the Fe-Pt binary system throughout the wide composition with minimal increments between compositions, we employed the combinatorial sputtering technique to deposit Fe-Pt composition-spread film. Details of the deposition method, as used in recent studies on the anomalous Hall/Nernst effects can be found in these references.[23–25] This combinatorial approach enables a high-throughput investigation of the transport properties of various Fe-Pt compositions within a single film, facilitating the identification of the optimal composition for the AHE sensor applications. In addition to the advantage in material development for practical sensor applications, this technique also allows for a comprehensive analysis of the fundamental mechanisms underlying the AHE based on systematic composition dependence. Thus, we analyzed the variation of AHE across the Fe-Pt composition comprehensively by comparing it with the result of the first-principles calculation of the AHC. Our results revealed an Fe-rich composition, $Fe_{0.70}Pt_{0.30}$ has a large ρ_{yx}^{A} of 4.5 μΩ cm, DR of 600 mT, and significant sensitivity of 8 μΩ cm/T. Based on the theoretical calculation, these properties would stem from an intrinsic mechanism driving large AHE and moderately large K_u.

II. METHODS

The $Fe_{1-x}Pt_x$ composition-spread film was deposited on a single-crystalline MgO(001) substrate with a size of 10×10 mm^2 at 450℃ using a combinatorial sputtering system (CMS-A6250X2, Comet, Inc.). The base pressure was about 5×10^{-6} Pa. Prior to loading, the substrate was cleaned by sequentially sonicating it in acetone, ethanol, and at the end in deionized (DI) water, each for 10 minutes. After loading the substrate, in-situ Ar-ion milling was carried out to remove residual surface contamination. The thickness of the films was calibrated with X-ray reflectivity (XRR) to control the deposition rate. A schematic diagram of the film is shown in Fig. 2 (a). A wedge-shaped layer of Fe and Pt, with the layer thickness of 0.4 nm per one-unit layer, was deposited in 75 times to achieve a final film thickness of 30 nm. The composition gradient width was set to 7 mm. After deposition, the sample was cooled down to room temperature, and a 2-nm thick Ta capping layer was deposited to prevent oxidization.

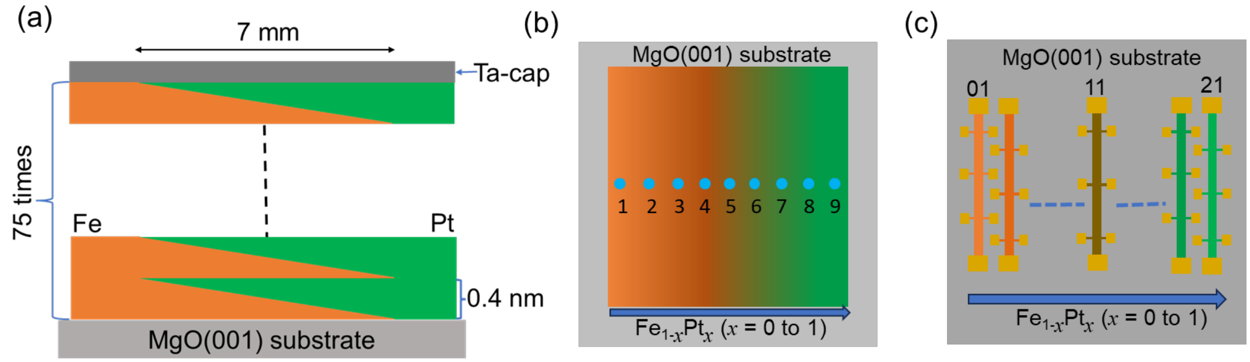

Fig. 2. Schematic diagrams for (a) side-view and (b) top-view of $Fe_{1-x}Pt_x$ composition-spread film on MgO(001) substrate. The 9 points where x-ray diffraction is performed using a 0.5 mm slit is indicated in part (b). (c) Schematic diagram of Hall bar from Fe to Pt side for Hall effect measurements.

To investigate the crystal structure, X-ray diffraction (XRD) was performed with a Cu K_α source and a two-dimensional detector (PILATUS 100K/R, Rigaku Co.) at 9 positions across the sample, from the Fe-rich to Pt-rich side with a 0.5 mm slit (Fig. 2(b)). XRR was also performed at 5 positions to determine the actual film thickness. For transport properties measurements, including anomalous Hall resistivity and longitudinal resistivity, the sample was patterned into Hall bars using photolithography and Ar-ion milling(Fig. 2(c)). The width of the Hall bar was designed to be 100 μm, which contains a small variation of the composition $\pm 0.57\ to\ 0.89$at.% within each bar, except the devices in the pure Fe and Pt. The AHE was measured at 300 K by sweeping a perpendicular magnetic field from 3 T to -3 T and back for each Hall bar using the Physical Property Measurement System (PPMS, Quantum Design Co., Ltd.). The longitudinal resistivity was also measured at room temperature.

For the calculation of AHC, we first obtained the electronic structures of bcc-Fe, L1_2-Fe$_3$Pt, and L1_0-FePt based on the density-functional theory, which is implemented in the Vienna *ab initio* simulation program (VASP). [26] Here, we considered the spin-orbit interaction to calculate the AHC. The generalized gradient approximation was used for the exchange correlation energy and the projector augmented wave pseudopotential was employed to treat the effect of core electrons appropriately.[27–29] The lattice constants were chosen as 2.86 Å for $A2$-Fe, 3.87 Å for $L1_2$-Fe$_3$Pt and 3.90 Å (a-axis) and 3.74 Å (c-axis) for $L1_0$-FePt. The magnetization direction was set along the [001] direction for all the systems. Using the obtained electronic structures, we calculated the AHC using the following expression derived by the linear response theory:

$$\sigma_{xy}(\varepsilon) = -\frac{e^2}{\hbar}\int \frac{d^3\boldsymbol{k}}{(2\pi)^3}\Omega^z\,(\boldsymbol{k}), \tag{1}$$

where $\Omega^z(\mathbf{k})$ is the Berry curvature given by

$$\Omega^z(\mathbf{k}) = -\left(\frac{\hbar}{m}\right)^2 \sum_n f\left(E_{n,\mathbf{k}}, \varepsilon\right) \sum_{n\neq n'} \frac{2\,\mathrm{Im}\langle\psi_{n,\mathbf{k}}|p_x|\psi_{n',\mathbf{k}}\rangle\langle\psi_{n',\mathbf{k}}|p_y|\psi_{n,\mathbf{k}}\rangle}{\left(E_{n',\mathbf{k}} - E_{n,\mathbf{k}}\right)^2}. \tag{2}$$

Here, p_x (p_y) is the x (y) component of the momentum operator, $\psi_{n,\mathbf{k}}$ represents the Block wave function with the eigenenergy$E_{n,\mathbf{k}}$, and $f(E_{n,\mathbf{k}}, \varepsilon)$ is the Fermi-Dirac distribution function. For the Brillouin-zone integration in Eq. (1), we used k points of 151 × 151 × 151 for bcc-Fe and 91 × 91 × 91 for $L1_2$-Fe$_3$Pt and $L1_0$-FePt confirming good convergence of $\sigma_{xy}(\varepsilon)$.

III. RESULTS AND DISCUSSION

A. Crystal structures

The crystal structures result is summarized in Fig. 3(a). By comparing these experimental XRD patterns with simulated ones (upper panel of Fig. 3(a)) and the Fe-Pt binary phase diagram[30] (Fig. 3 (b)), the epitaxial growth in the [001] direction of either $A2$-Fe, $L1_2$-Fe$_3$Pt, $L1_0$-FePt, or $L1_2$-FePt$_3$ was confirmed in almost all composition regions except for Pt-rich region.

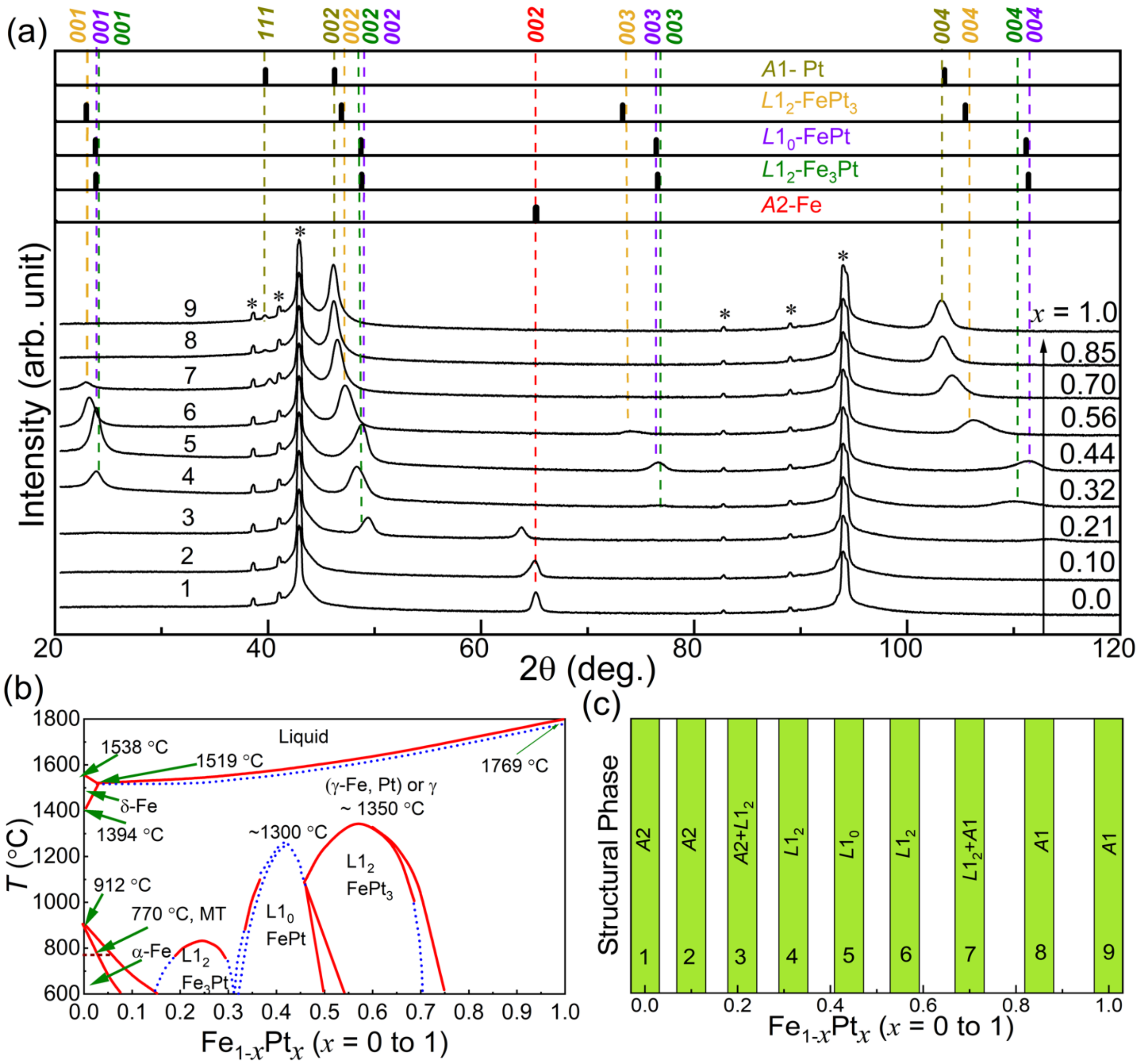

Fig. 3 (a) Experimental XRD patterns across the $Fe_{1-x}Pt_x$ composition spread film, along with peak indices and comparison with simulated XRD patterns. The peaks corresponding to the MgO(001) substrate are marked with asterisks in the XRD patterns. (b) Phase diagram of Fe-Pt binary system[30], (c) Structural phases obtained from the analytical comparison between simulated and experimental XRD patterns.

In the composition region up to $x = 0.10$, only the 002 peak from *A*2-Fe was observed. From $x = 0.32$ to 0.70, only diffraction peaks were observed at the 2θ close to the simulated peak positions originating from {001}-planes of $L1_2$-Fe_3Pt, $L1_0$-FePt and $L1_2$-$FePt_3$ phases. Notably, *001* superlattice peak at 23° to 25° clearly indicates the formation of these ordered phases. Although it is difficult to distinguish specific phases at each composition, based on slight shifts of the peak positions and the magnetic properties from AHE measurement (shown later in Fig. 4), we concluded the following phase distinctions: (i) At $x = 0.32$, $L1_2$-Fe_3Pt is the primary phase, showing small perpendicular magnetic anisotropy (PMA). (ii) At $x = 0.44$, the main phase transitions to $L1_0$-FePt , exhibiting strong PMA. (iii) At $x = 0.56$, the phase changed to $L1_2$-$FePt_3$, evidenced by a large shift in the diffraction peak position. For the composition range $x \geq 0.85$, the phase becomes a single disordered *A*1 structure. The insufficient deposition temperature is the reason to not have epitaxial film in Pt rich region and the presence of *111* peak as reported by Kun ho et al. [31], where it reported growing Pt in [001] direction, the deposition temperature must be more than 500 ℃. In the intermediate regions, the coexistence of *A*2-Fe(*A*1-Pt) and $L1_2$-Fe_3Pt ($L1_2$-Fe_3Pt) was confirmed for $x = 0.21(0.70)$. It should be noted that the detection of mixed phases can be attributed to the relatively wide width (0.5 mm) of the incident slit of XRD, which should contain structural information of the composition range of ±6 at.%. The structural phases determined by comparing the experimental XRD patterns with the simulated ones are summarized in Fig. 3 (c). The phase is shown in the bar diagram due to the width of the composition covered by XRD slit 0.5 mm. It can be seen that the identified phases in the present composition spread film agreed well with the phase diagram shown in Fig.3 (b).

B. Hall resistivity, saturation field and coercivity

The perpendicular field dependence of the Hall resistivity (ρ_{yx}) of the composition-spread film from x = 0 to 0.08, 0.12 to 0.30, 0.35 to 0.65 and 0.70 to 1.0 are shown in Fig. 4(a-d), respectively. It is found that the films with compositions ranging up to x = 0.30 did not exhibit coercivity, which is suitable for AHE sensor applications. On the other hand, it is evident from films with compositions x = 0.35 to x = 0.65 exhibit a clear hysteresis curve and coercivity, which should be attributed to large K_u in $L1_0$-FePt phase. The coercivity finally disappeared in x ≥ 0.70 as shown in Fig. 4(d).

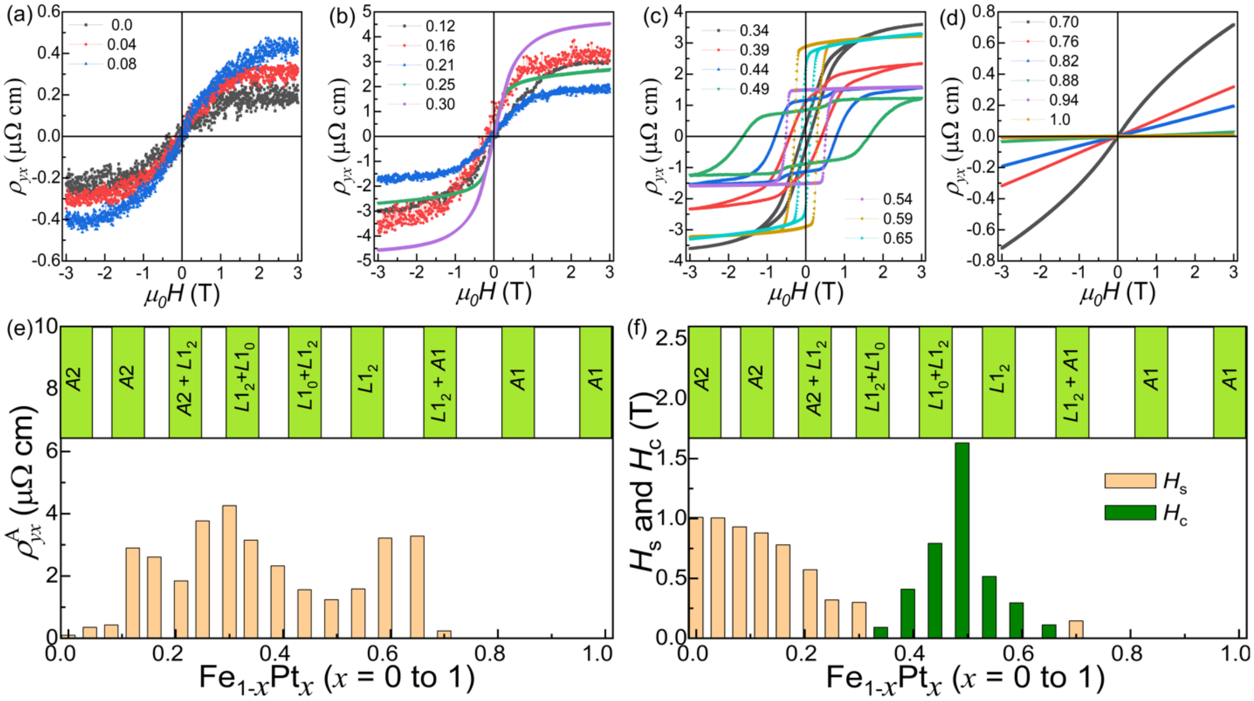

Fig. 4(a-d)Magnetic field dependent Hall resistivity (ρ_{yx}) of the Fe$_{1-x}$Pt$_x$ composition-spread film measured at 300 K. Composition dependence of (e) anomalous Halll resistivity (ρ^A_{yx}) and (f) saturation field (H_s) and coercivity (H_c).

The ρ^A_{yx} , which is the most important parameter for AHE sensors, was evaluated using the formula $\rho_{yx} = \rho_0 H + 4\pi R_S M_S = \rho_{OH} + \rho^A_{yx}$, where the first term is originated from the OHE and the second term is the AHE. The second term is obtained from the extrapolation of the Hall curve from high field to zero. The result is summarized in Fig. 4(e). The value of ρ_{yx}^{A} of pure Fe ($x = 0$) was 0.1 μΩ cm, consistent with the previous study.[32] By adding Pt, ρ_{yx}^{A} increased to 2.9 μΩ cm at $x = 0.12$ and reached a maximum of 4.3 μΩ cm at $x = 0.30$ where the main phase was identified as $L1_2$-Fe_3Pt. The ρ_{yx}^{A} then drops to 1.2 μΩ cm at $x = 0.49$ in the region of the $L1_0$-FePt phase. From $x = 0.49$ to 0.65, it again increased and reached 3.3 μΩ cm then decreased to become zero for x >0.70 due to paramagnetic nature. This oscillatory tendency of the ρ_{yx}^{A} with x was qualitatively explained by the intrinsic anomalous Hall conductivity originating from the electronic structure and the effect of Fermi level shifting, which will be discussed later.

The H_s, another important parameter for AHE sensors, was analyzed only for the composition regions exhibiting no hysteresis loop. A linear fit was performed for higher and lower magnetic field regions, and the intersecting point was defined as H_s. The results are summarized in Fig. 4(f). For pure Fe ($x = 0.0$), the H_s found to be large ≈ 1100 mT. As increasing x, H_s decreases to a minimum value of ≈ 320 mT at $x = 0.30$, where almost no coercivity was observed. The lowest H_s coincided with the largest ρ_{yx}^{A} for the composition $x = 0.30$, where the main phase was found to be $L1_2$-Fe_3Pt. The H_c for different compositions, where clear hysteresis was observed, is also shown in Fig. 4(f). The H_c was evaluated using $H_c = |(H_1 - H_2)|/2$, where H_1 and H_2 are the lower and upper cut-off fields at which the Hall resistivity becomes zero. The H_c is found to be maximum ≈ 1800 mTfor $x \approx 0.50$, as expected from the previous report.[33] The increase in H_c with Pt should be due to a higher proportion of the $L1_0$ phase than that of the $L1_2$ phase. For $x > 0.5$, H_c starts to decrease after the transition from the $L1_0$ to $L1_2$ phase. From $x \geq 0.75$, the sample becomes a paramagnetic, containing the $A1$ phase. We also measured the longitudinal resistivity, which is shown in Fig. SI1. The resistivity of all compositions is consistent with the previous report by Q. Hao et. al..[34]

C. Evaluation of anomalous Hall sensitivity and dynamic range

In order to evaluate the property as an AHE sensor, we analyzed the composition dependence of *S* and *DR* in the $Fe_{1-x}Pt_x$ composition spread film. *S* was evaluated by analyzing the slope of Hall resistivity ($S = d\rho_{yx}/dH$). The highest *S* obtained in the *H*ext dependence of *S* (S_{max}) for each composition is summarized in Fig. 5(a). The S_{max} for pure Fe ($x = 0.0$) was estimated to be as small as, 0.21 μΩ cm/T. The S_{max} rapidly increases to 3.58 μΩ cm/T at $x = 0.16$, which is due to the large enhancement of ρ_{yx}^{A} and the reduction of H_s. The S_{max} shows an almost monotonic increase with *x* and shows maximum value of 8 μΩ cm/T at $x = 0.30$. The inset in Fig. 5(a) shows the field dependence of the *S* for $x = 0.30$, which shows the S_{max} at near zero field range. Figure 5(b) shows the *x* dependence of the *DR*. Although we defined $DR = 2H_S$ in Fig.1 for the ideal case showing the linear change in ρ_{yx} up to H_s, we found non-linear behavior in present Fe-Pt composition spread film. Therefore, here we have considered 5 % non-linearity while evaluating *DR* as shown in inset of Fig. 5(b) for on e of the composition $x = 0.30$. The non-linearity commonly expressed as a percentage of the full-scale (FS) output and in this paper non-linearity was determined using $\left|\rho_{yx}(\mu_0 H) - \rho_{yx}^{Fit}(\mu_0 H)\right| / (\rho_{yx}^{max}(\mu_0 H) - \rho_{yx}^{min}(\mu_0 H)) \times 100\%\mathrm{FS}$, where $\rho_{yx}(\mu_0 H)$, $\rho_{yx}^{Fit}(\mu_0 H)$ are experimental observed Hall resistivity and its linear fit curve, $\rho_{yx}^{max}(\mu_0 H), \rho_{yx}^{min}(\mu_0 H)$ are Hall resistivity at maximum and zero field. The maximum *DR* value of 1400 mT was observed for $x = 0.0$, followed by rapid decrease to 630 mT at 0.12, then increased to 1200 mT at $x = 0.16$. From $x = 0.16$ to 0.30 it again monotonically decreases 600 mT. It is noteworthy that the present study based on the $Fe_{1-x}Pt_x$ composition-spread film demonstrates the largest S_{max} with a relatively large *DR* for the Fe-rich composition of $Fe_{0.70}Pt0_{.30}$, which can be originated from the combination of large AHC in $L1_2$-Fe_3Pt and large K_u in $L1_0$-FePt. In addition, we also successfully tuned the *DR* in a wide range from 600 to 1400 mT in single binary alloy system by controlling K_u and $M_s^2\mu_0/2$.

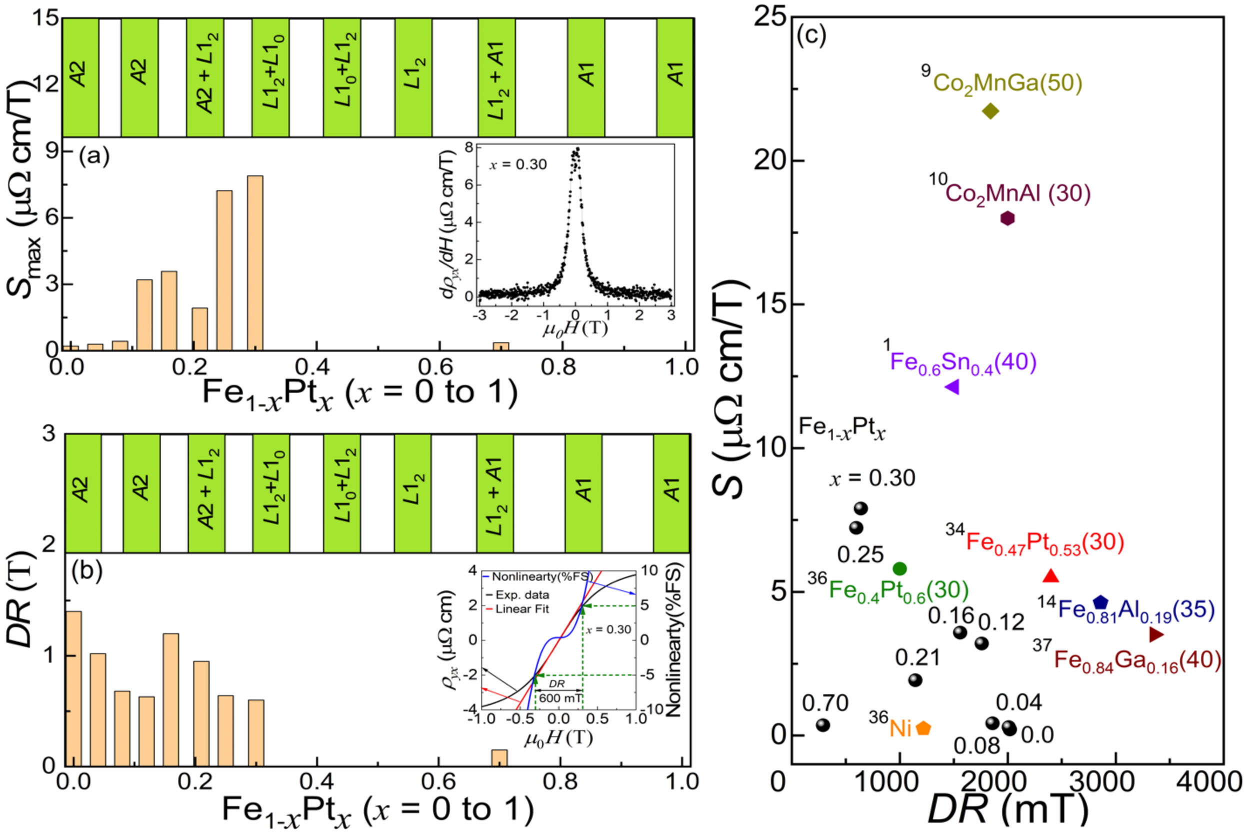

Fig. 5. Composition dependence of (a) maximum anomalous Hall sensitivity ($S_{\max}$) and, (b) *DR* in the the $Fe_{1-x}Pt_x$ composition-spread film. (c) *S* and *DR* for different magnetic materials reported in the literature and the result of the present study for the Fe-Pt binary compositions. Inset of (a) and (b) represent the magnetic field dependence of the $d\rho_{yx}/dH$ and the evaluation process of DR based on the non-linearity for $x = 0.30$, respectively.

Fig. 5(c) shows the *S* and *DR* of various materials reported in the previous studies[1,9,10,14,34–37], along with the results obtained in this study. Although the present study could not realize the *S* larger than some topological materials such as Co_2MnGa, Co_2MnAl and $Fe_{0.6}Sn_{0.4}$, the relatively large *S* of 8 μΩ cm/T and *DR* of 600 mT were achieved for Fe-rich $Fe_{0.70}Pt_{0.30}$ composition.

D. Analysis of the Fe-Pt composition dependence of anomalous Hall conductivity (AHC)

Finally, in order to understand the mechanism of the x dependence of AHE in Fe-Pt composition-spread film, we evaluated the anomalous Hall conductivity (AHC) using $\sigma_{xy}^{A} = \rho_{yx}^{A}/\left(\left(\rho_{yx}^{A}\right)^{2} + (\rho_{xx})^{2}\right)$formula and AHC with x dependence is shown in Fig. 6(a). The variation of AHC with x shows complex behavior. The AHC for pure Fe ($x = 0$) was 910 S/cm , but it sharply decreased to 480 S/cm by adding a small amount of Pt ($x = 0.04$), while keeping the *A*2 structure. With increasing x, the AHC increased to 1008 S/cm at $x = 0.16$ then reduced to 494 S/cm for $x = 0.20$ in the region where the $L1_2$ phase started to form. As the composition become close to stoichiometric $L1_2$-Fe_3Pt ($x = 0.30$), the AHC reached a peak value of 1261 S/cm. Finally, the AHC reduces to 494 S/cm at $x = 0.49$ in the pure $L1_0$ phase region. In order to uncover this non-monotonic change in the experimental AHC with x from the viewpoint of intrinsic mechanism, we performed the theoretical calculations of AHC for three specific compositions with ideal structures of *A*2-Fe, $L1_2$-Fe_3Pt, and $L1_0$-FePt. The energy dependence of intrinsic σ_{xy} is shown in Fig. 6(b). The values of σ_{xy} in *A*2-Fe, $L1_2$-Fe_3Pt, and $L1_0$-FePt phases at the Fermi level (E_F) were obtained as 776 S/cm, 1759 S/cm and 858 S/cm respectively, which are relatively close to the experimental σ_{xy}^{A} at around $x = 0.0$, 0.30 and 0.49 as shown in Fig.6(a). This suggests that the main origin of AHE in these three compositions could be an intrinsic mechanism and large S obtained at $x = 0.30$ originates from large intrinsic σ_{xy} . It should be noted that the difference in the temperature (0 K for theoretical σ_{xy} and 300 K for experimentalσ_{xy}^{A}) can be a reason for a quantitative disagreement. Here, we also noticed a similar behavior between the theoretical and experimental σ_{xy} in all the three structures . It can be found from Fig. 6(b) that the theoretical σ_{xy} decreases by giving small positive shifting of the energy (less than 100 meV) from the E_F in all three phases. Similarly, we found the reduction of the experimental σ_{xy}^{A} with increasing x from each x = 0.0, 0.30 and 0.49. This similarity motivated us to investigate the effect of Pt addition in $A2$-Fe, $L1_2$-Fe_3Pt and $L1_0$-FePt on the position of E_F. As the theoretical calculation of the AHC in off-stoichiometric composition is usually technically difficult, we performed the density of states (DOS) calculation of Fe-Pt compositions considering the $A2$ and $L1_2$structures using the AkaiKKR code based on the density-functional theory and the Korringa-Kohn-Rostoker (KKR) method.[38,39] It can be seen from the spin-revolved DOS calculation (see Fig. SI2(a and b)) that Pt addition works as electron doping while keeping the total shape of DOS like a rigid-band model. Therefore, we concluded that the effect of small amounts of Pt doping on AHC for $A2$-Fe and $L1_2$-Fe_3Pt may be explained by the intrinsic mechanism in combination with the rigid-band model, where the Pt doping plays a role of the electron doping into stoichiometric $A2$-Fe and $L1_2$-Fe_3Pt[23] However, certain trends, such as the increase of AHC around x = 0.16, are not fully explained by the intrinsic mechanism alone. This comprehensive analysis of AHC in the Fe-Pt composition-spread film has provided insight into some of the dominant origins of this phenomenon. For more rigorous analysis, future studies should include temperature-dependent AHE across the composition regions and clarification of its origins (both intrinsic and extrinsic origins) based on the scaling analysis.

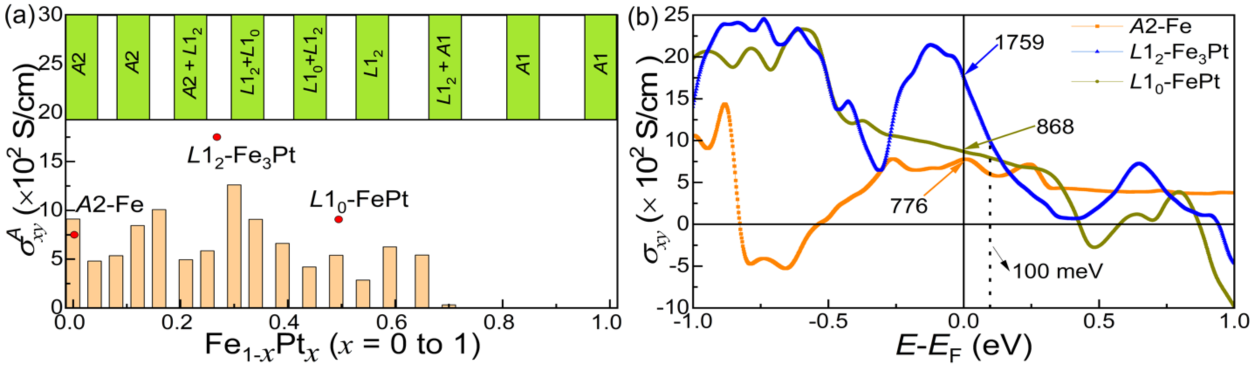

Fig. 6. Composition dependence of (a) anomalous Hall conductivity (AHC; σ_{xy}^{A}), red points represent the theoretically calculated σ_{xy} at E_F, (b) theoretical AHC (σ_{xy}) of $A2$-Fe, $L1_2$-Fe_3Pt, and $L1_0$-FePt.

IV. CONCLUSION

The composition dependence of the AHE in $Fe_{1-x}Pt_x$ ($0 \leq x \leq 1$) composition-spread film was investigated systematically, aiming to obtain large sensitivity for magnetic field sensors while understanding the underlying physical mechanisms. The film exhibited epitaxial growth with distinct phases such as $A2$-Fe, $L1_2$-Fe_3Pt, $L1_0$-FePt, and $L1_2$-$FePt_3$. The Fe-rich $Fe_{0.70}Pt_{0.30}$ composition shows the largest ρ_{yx}^{A} of 4.5 μΩ cm, with a linear response to the magnetic field, resulting in a high *S* of 8 μΩ cm/T and *DR* of 600 mT. The *DR* can be tuned between 600 and 1400 mT by adjusting the Fe:Pt composition ratio, which was attributed to the variations in the magnetic anisotropy and magnetization of the system. The experimental AHC also varied with composition, exhibiting a peak value of 1261 S/cm for $Fe_{0.70}Pt_{0.30}$. The theoretical analysis of the AHC for the $A2$-Fe and $L1_2$-Fe_3Pt, along with an analysis of the DOS for off-stoichiometric compositions, indicates that the overall variation in AHC with *x* can largely be attributed to an intrinsic mechanism and the electron doping effect introduced by Pt addition. Theoretical analysis also supports that the $Fe_{0.70}Pt_{0.30}$ achieves the highest *S* due to its large intrinsic AHC in the $L1_2$-Fe_3Pt.

Acknowledgments

This work was supported by JST CREST (Grant No. JPMJCR21O1), JST ERATO "Magnetic Thermal Management Materials" (Grant No. JPMJER2201), MEXT Program: Data Creation and Utilization-Type Material Research and Development Project (Digital Transformation Initiative Center for Magnetic Materials; Grant No. JPMXP112271), JSPS KAKENHI Grants-in-Aid for Scientific Research (B) (Grant

No. JP21H01608). Theoretical calculations in this work were performed on the Numerical Materials Simulator at NIMS.

Supplementary material

See the supplementary material for additional data.

Author Declarations

The authors have no conflicts to disclose.

Data Availability Statement

The data supporting the findings of this study are available from the corresponding author upon reasonable request.

References

[1] Y. Satake, K. Fujiwara, J. Shiogai, T. Seki, and A. Tsukazaki, Sci. Rep. **9**, 3282 (2019).

[2] K. Wang, Y. Zhang, and G. Xiao, Phys. Rev. Appl. **13**, 064009 (2020).

[3] Y. Zhu, and J.W. Cai, Appl. Phys. Lett. **90**, 012104 (2007).

[4] W.L. Peng, J.Y. Zhang, L.S. Luo, G.N. Feng, and G.H. Yu, J. Appl. Phys. **125**, 093906 (2019).

[5] W. Su, Z. Hu, Y. Li, Y. Han, Y. Chen, C. Wang, Z. Jiang, Z. He, J. Wu, Z. Zhou, Z. Wang, and M. Liu, Adv. Funct. Mater. **33**, 2211752 (2023).

[6] Y. Zhang, Q. Hao, and G. Xiao, Sensors **19**, 3537 (2019).

[7] Y.M. Lu, J.W. Cai, H.Y. Pan, and L. Sun, Appl. Phys. Lett. **100**, 022404 (2012).

[8] T. Nakatani, P.D. Kulkarni, H. Suto, K. Masuda, H. Iwasaki, and Y. Sakuraba, Appl. Phys. Lett. **124**, 070501 (2024).

[9] K. Sumida, Y. Sakuraba, K. Masuda, T. Kono, M. Kakoki, K. Goto, W. Zhou, K. Miyamoto, Y. Miura, T. Okuda, and A. Kimura, Commun. Mater. **1**, 89 (2020).

[10] Y. Sakuraba, K. Hyodo, A. Sakuma, and S. Mitani, Phys. Rev. B **101**, 134407 (2020).

[11] L. Ye, M. Kang, J. Liu, F. von Cube, C.R. Wicker, T. Suzuki, C. Jozwiak, A. Bostwick, E. Rotenberg, D.C. Bell, L. Fu, R. Comin, and J.G. Checkelsky, Nature **555**, 638 (2018).

[12] S. Nakatsuji, N. Kiyohara, and T. Higo, Nature **527**, 212 (2015).

[13] A. Sakai, S. Minami, T. Koretsune, T. Chen, T. Higo, Y. Wang, T. Nomoto, M. Hirayama, S. Miwa, D. Nishio-Hamane, F. Ishii, R. Arita, and S. Nakatsuji, Nature **581**, 53 (2020).

[14] W. Zhou, and Y. Sakuraba, Appl. Phys. Express **13**, 043001 (2020).

[15] Y. Wang, C. Li, H. Zhou, J. Wang, G. Chai, and C. Jiang, Appl. Phys. Lett. **118**, 071902 (2021).

[16] X. Zheng, X. Zhao, J. Qi, X. Luo, S. Ma, C. Chen, H. Zeng, G. Yu, N. Fang, S.U. Rehman, W. Ren, B. Li, and Z. Zhong, Appl. Phys. Lett. **118**, 072402 (2021).

[17] T. Zhu, P. Chen, Q.H. Zhang, R.C. Yu, and B.G. Liu, Appl. Phys. Lett. **104**, 202404 (2014).

[18] Y. Zhang, K. Wang, and G. Xiao, Appl. Phys. Lett. **116**, (2020).

[19] M. Li, H. Pi, Y. Zhao, T. Lin, Q. Zhang, X. Hu, C. Xiong, Z. Qiu, L. Wang, Y. Zhang, J. Cai, W. Liu, J. Sun, F. Hu, L. Gu, H. Weng, Q. Wu, S. Wang, Y. Chen, and B. Shen, Adv. Mater. **35**, 2301339 (2023).

[20] S. Xiao, D. Zhang, and N. Wang, J. Phys. D. Appl. Phys. **56**, 454001 (2023).

[21] M. Watanabe, and T. Masumoto, Thin Solid Films **405**, 92 (2002).

[22] K. Wang, Y. Zhang, S. Zhou, and G. Xiao, Nanomaterials **11**, 854 (2021).

[23] R. Toyama, K. Masuda, K. Simalaotao, W. Zhou, V.K. Kushwaha, and Y. Sakuraba, J. Phys. D. Appl. Phys. **57**, 405001 (2024).

[24] R. Toyama, W. Zhou, and Y. Sakuraba, Phys. Rev. B **109**, 054415 (2024).

[25] R. Modak, K. Goto, S. Ueda, Y. Miura, K. Uchida, and Y. Sakuraba, APL Mater. **9**, 031105 (2021).

[26] G. Kresse, and J. Furthmüller, Phys. Rev. B **54**, 11169 (1996).

[27] J.P. Perdew, K. Burke, and M. Ernzerhof, Phys. Rev. Lett. **77**, 3865–3868 (1996).

[28] P.E. Blöchl, Phys. Rev. B **50**, 17953–17979 (1994).

[29] G. Kresse, and D. Joubert, Phys. Rev. B **59**, 1758–1775 (1999).

[30] P. Entel, M.E. Gruner, G. Rollmann, A. Hucht, S. Sahoo, A.T. Zayak, H.C. Herper, and A. Dannenberg, Philos. Mag. **88**, 2725 (2008).

[31] K.H. Ahn, S. Baik, and S.S. Kim, J. Mater. Res. **17**, 2334 (2002).

[32] Y. Tian, L. Ye, and X. Jin, Phys. Rev. Lett. **103**, 087206 (2009).

[33] T. Shima, K. Takanashi, Y.K. Takahashi, and K. Hono, Appl. Phys. Lett. **85**, 2571 (2004).

[34] Q. Hao, W. Chen, S. Wang, and G. Xiao, J. Appl. Phys. **122**, 033901 (2017).

[35] A. Gerber, A. Milner, A. Finkler, M. Karpovski, L. Goldsmith, J. Tuaillon-Combes, O.

Boisron, P. Mélinon, and A. Perez, Phys. Rev. B **69**, 224403 (2004).

[36] G.X. Miao, and G. Xiao, Appl. Phys. Lett. **85**, 73 (2004).

[37] H. Nakayama, K. Masuda, J. Wang, A. Miura, K. Uchida, M. Murata, and Y. Sakuraba, Phys. Rev. Mater. **3**, 114412 (2019).

[38] J. Korringa, Physica **13**, 392 (1947).

[39] W. Kohn, and N. Rostoker, Phys. Rev. **94**, 1111 (1954).